Architected Tungsten Carbide Electrodes using Origami Techniques

Monsur Islam, Devin Keck and Rodrigo Martinez-Duarte*

M. Islam, D. Keck, and R. Martinez-Duarte
Multiscale Manufacturing Laboratory, Mechanical Engineering Department, Clemson University, Clemson, SC 29634, USA
Email address: rodrigm@clemson.edu (R. Martinez-Duarte)

M. Islam
Institute for Microstructure Technology, Karlsruhe Institute of Technology, Hermann-von-Helmholtz-Platz 1, Eggenstein-Leopoldshafen 76344, Germany

ABSTRACT

We present the fabrication of 3D complex shapes of porous tungsten carbide (WC) using an origami-inspired manufacturing technology. This is the first report of this technology, which allows for the fabrication of complex WC structures featuring a density as low as 0.06 g/cm^3. The porous WC origami structures are fabricated by heat treatment of folded paper infiltrated with an aqueous solution of ammonium metatungstate (AMT). WC purity up to 96% was achieved when using an AMT concentration of 20%, synthesis temperature of 1300 °C and heating rate of 2.5 °C/min. The as synthesized WC featured a BET surface area of 102.06 m^2/g. Beyond obtaining high purity WC, the focus was on understanding the effect of the microstructure on the mechanical performance of origami structures. Increasing the purity of WC decreased the elastic modulus and compressive strength of the origami structure, which is attributed to the increasing grain size of the crystalline phase materials and increase of graphitic phases in carbon with increasing temperature. Furthermore, the WC origami structures exhibited good and stable electrical conductivity under compressive stress. These initial results, coupled to the excellent electrochemical properties of the WC system, encourage further work on using paper as a scaffold to fabricate origami-inspired multifunctional structures, for structural energy components.

Keywords: Tungsten carbide, Origami, Cellulose, Lightweight material, Architected electrode.

1. INTRODUCTION

Tungsten carbide (WC) is a transition metal carbide that features platinum-like electrocatalytic properties at a reduced cost.[1] A further advantage of WC over platinum is that, unlike platinum, WC does not get inactivated by common poisons such as hydrogen sulphide (H_2S) and carbon monoxide (CO) during hydrogen oxidation reaction, and even promotes effective electrooxidation of these compounds[2]. Furthermore, WC exhibits stability in a wide range of pH and temperatures.[3]–[6] These properties have established WC as a suitable alternative to platinum as electrode material in various applications including microbial fuel cells and batteries.[7]–[12] The excellent mechanical properties of WC are also well established. For example, the compression strength and Young's modulus of bulk WC are among the highest known, around 400 MPa and 700 GPa respectively, while also featuring high hardness, wear-resistance, and high temperature strength and hardness[13]–[15]. Thanks to such mechanical and electrochemical properties, WC shows excellent potential as a structural electrode material towards multifunctional devices such as structural fuel cells and batteries to meet future needs in portable electronics, aerospace and hybrid ground transports.[16]–[20] In such context, structural WC electrodes will also benefit from porosity, both to decrease their weight and to increase their surface area and reactivity. Although porous WC is routinely derived by powder sintering or heat treatment of bio-templates, i.e. wood, peels, infiltrated with tungsten salts or particulates,[21][22] structuring WC has proven difficult because of the poor workability of pressed WC sheets, limitations on complexity due to geometry of the pressing mold, or lack of control over the available shape factor of the bio-template.

To this end, here we present for the first time the use of origami folding techniques to enable the derivation of WC structured electrodes. Origami is an ancient Japanese art of paper folding, where a 3D complex shape can be fabricated from a 2D paper by folding it along prescribed crease lines, and is now recognized as a framework for the design of mechanical structures of tailorable properties.[23]–[26] In this work we used commercial and widely available pure cellulosic paper, a renewable resource, as a base material. Once structured using origami designs, we infiltrated it with Ammonium Meta Tungstate (AMT), a tungsten (W) salt, and then treated it to temperatures up to 1300 °C in an inert atmosphere. During this process, the cellulosic paper carbonized, tungsten was derived from its salt and finally carbon and tungsten reacted to form WC. In this first report of WC origami, we focus on elucidating the effect of processing on the mechanical and electrical properties of the structures and characterizing the electrical stability of the WC structured electrodes under a mechanical load. We emphasize mechanical properties to complement several works by other authors on the effect of processing on the electrochemical performance of WC.[1][7][12][27] Different process variables were studied to understand their impact on the final composition and mechanical properties of WC origami. We first present the fabrication process and then how the concentration of a W salt, and both temperature and heating rate during heat treatment determine the composition and crystallinity of WC origami. We then report on the mechanical and electrical properties of Miura-ori origami structures with a dominant phase of WC, with the goal of elucidating the impact of material properties and microstructure on the origami macro-structure.

2. MATERIALS AND METHODS

2.1 Design of Experiment (DOE)

A DOE and Taguchi methods were implemented using Minitab (Minitab Inc, USA) software to optimize the conditions for the synthesis of WC from chromatography paper. Experiments were planned using an orthogonal array as obtained by the Minitab software proposed by the Taguchi method. Minitab was also used to analyze results using Analysis of Variance (ANOVA). The orthogonal array provided different combinations of parameters and their levels for each experiment. According to the Taguchi method, the orthogonal array allows for the study of the entire parameter space with a minimum number of experiments.[28] The synthesis parameters studied in this work were concentration of AMT, final temperature during heat treatment, and the heating rate. Three levels of each parameter were chosen here as shown in Table 1.

Table 1: Levels of the synthesis parameters used for the Taguchi method

Parameters	Level 1	Level 2	Level 3
Temperature	1100 °C	1200 °C	1300 °C
Heating rate	1 °C/min	2.5 °C/min	5 °C/min
AMT	10%	20%	50%

L9 orthogonal arrays were chosen for three synthesis parameters and three levels for each parameter. Such arrays provided nine set of experiments with best combinations of the synthesis parameters to study the results within the entire design space (see Table S1 in the supplementary information). The output signal chosen in this study was the relative amount of WC obtained after heat treatment, as our aim was to optimize the parameters for the synthesis of WC with the highest purity. The relative amount of WC in the samples was determined using Equation 1 (i.e. *X*=WC). Three forms of signal to noise (S/N) ratio can be used to analyze the results following the Taguchi method: smaller-the-better, nominal-the-better, and larger-the-better. The larger-the-better S/N ratio was chosen in this study, as the relative amount of WC should be highest at the optimum conditions. For the larger-the-better condition, the S/N is determined by Equation 2.[29] Table S1 (See the supplementary information) details the L9 orthogonal arrays and the corresponding results. Analysis of Variance (ANOVA) was implemented with Minitab and used to analyze the effect of synthesis parameters on the output signal, or relative amount of WC.

$$Relative\ amount\ of\ X = \frac{Sum\ of\ the\ intensites\ of\ the\ peaks\ for\ X\ in\ XRD}{Sum\ of\ the\ intensities\ of\ all\ the\ peaks\ present\ in\ XRD} \times 100\% \quad \text{Equation 1}$$

$$S/N = -10 \log \left[mean\ of\ sum\ of\ squares\ of\ reciprocal\ of\ measured\ data\right] \quad \text{Equation 2}$$

2.2 Materials

Pure cellulose chromatography paper (Fisherbrand Chromatography Paper, Sigma Aldrich, Cat. No. 05-714-1) with a thickness of 0.19 mm was used for this work. Ammonium metatungstate (AMT, Sigma Aldrich, Cat. No. 463922) was used as the tungsten precursor for WC synthesis. We used ultra-pure water as the solvent of the AMT solution used to infiltrate the paper.

2.3 Fabrication of WC origami

Figure 1 presents the general fabrication process of a WC origami shape. Among different origami shapes, Miura-ori has gained much attention because of its simplicity and high specific stiffness.[26][30] In the context of structural electrodes, the Miura-ori geometry (Figure 1) offers a rigid structure with an open cell geometry, to facilitate transport of electrolyte for example, and increased surface area. Hence, in this work we emphasized the fabrication of Miura-ori structure. The inset of Figure 1a shows the crease pattern for a unit cell of a Miura-ori fold. The dotted and solid lines in the unit cell represented the creases to create "valleys" on one side of the paper and "mountains" on the other. The Miura-ori design used here featured 16 unit cells. A unit cell of Miura-ori was defined by the design parameters h, l and α.[31] All the Miura-ori samples fabricated in this work featured an α of 75°, an h of 9.18 mm and a 3:5 ratio between h and l. We designed individual crease patterns for "valleys" and "mountains" for the origami structures using Solidworks (Dassault Systems, Waltham, MA, USA). The fabrication process started with pre-creasing the chromatography paper using an empty, generic ball point pen mounted on a desktop cutting-plotter machine (Graphtec CE6000-40, Japan). The ball point pen featured a ball diameter of 1.5 mm. The parameters used during the pre-creasing were: speed = 12 cm/s, acceleration = 0.71 m/s^2, force = 2.16 N, and number of passes = 3. An example of the pre-creased paper for Miura-ori in such process is shown in Figure 1a. Alignment of valleys and mountains was implemented using marks that were automatically generated by the software of the cutting plotter and printed on the paper.

The paper was infiltrated with AMT after pre-creasing using a given aqueous solution of AMT with different concentration (wt/vol.%). We immersed each sample of pre-creased paper in the AMT solution for 20 minutes. The samples were then dried on a hot plate at 85 °C for 1 hour to enable manual folding. An example of the folded paper Miura-ori previous to heat treatment is illustrated in Figure 1b.

2.4 Heat treatment

Once folded, the Miura-ori structures were heat treated in a tube furnace (TF1700, Across International, USA). The heat treatement protocol featured 5 steps: (1) heating from room temperature to 300°C at 5°C/min; (2) dwell at 300°C for 30 min to allow the excess oxygen to escape the furnace;[32][33] (3) heating from 300°C at various heating rates (1, 2.5 and 5°C/min) to a final temperature (800, 900, 1000, 1100, 1200 and 1300°C); (4) dwell at this temperature for 3 hours; and (5) cooling down to room temperature at a cooling rate of 5°C/min. Different final temperatures and heating rate were used in step (3). The dwell time in step (4) was kept constant at 3 hours, as a dwell time more than 3 hours does not have an effect on the synthesis of WC from biopolymers.[34] The entire heat treatment process was performed under a vacuum atmosphere since AMT contains a highly stable form of WO_3 that requires higher energy to break the stable W–O bond.[35] A vacuum environment provides higher energy to a sample by enabling higher sample temperature than any inert gas environment.[36] An example of the resultant Miura-ori after heat-treatment is shown in Figure 1c.

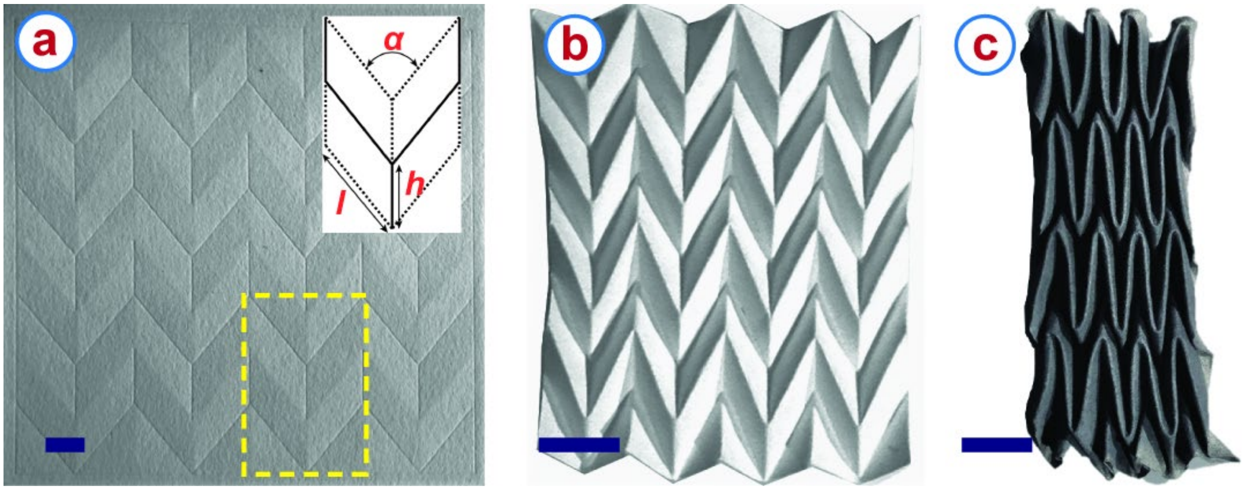

Figure 1: (a) Pure cellulose paper pre-creased using a plotter machine. The inset shows the geometry of a unit cell of a Miura-ori structure described by l, h and α. The unit cell is indicated on the paper by the dashed rectangle. (b) Paper Miura-ori structure after manually folding pre-creased paper. (c) A WC Miura-ori shape obtained after infiltrating the paper Miura-ori with 20% AMT and heat treating it to 1300°C at a heating rate of 2.5°C/min in vacuum. The scale bars in all figures represent 1 cm.

2.5 Material and microstructure characterization

All the samples obtained after heat treatment were characterized in terms of composition of crystalline materials using X-ray diffraction (XRD, Rigaku Ultima IV, Japan) using a diffractometer equipped with graphite monochromatized high intensity Cu Kα1 radiation (λ=

1.5405 Å). The microstructure of selected samples was characterized using scanning electron microscopy (SEM, S4800, Hitachi, Japan) and high resolution transmission electron microscopy (HRTEM, H9500, Hitachi, Japan). Elemental analysis of selected samples was performed using energy-dispersive X-ray spectroscopy (EDS, Oxford Instruments, US) mounted on a scanning electron microscope (SU6600, Hitachi, Japan). We characterized the size of the macropore (pore diameter >50 nm) between the fibers by image analysis of the SEM images using the Particle Analyzer macro built into the ImageJ software. For internal porosity measurement, we performed nitrogen adsorption-desorption at 77.35K using Quantachrome Autosorb iQ gas sorption analyzer (Quantachorme Instruments, USA). The Brunauer–Emmett–Teller (BET) method was used to measure the specific surface area of the heat-treated samples. The grain size of crystalline materials present in the heat treated samples was estimated from the XRD patterns using the Scherrer Equation. In the Scherrer equation (Equation 3), the avergae grain size (D) is estimated using the wavelength of X-ray (λ), the Bragg angle (θ), the half width of the diffracttion peak (B) and a constant *k*.[37] For a particular peak, θ was obtained by dividing the x-coordinate (i.e. 2θ) of the corresponding peak in the XRD pattern by 2. B was obatined by measuring the width of a peak at the correspodning 2θ at the half of the height of the peak. The constant *k* is a dimensionless shape factor, which depends on the shape of the crystallites. Scherrer calculated the value of k as $2(\ln 2/\pi)^{0.5} = 0.9395$ when assuming cube shaped crystallites.[37] However, depending on the shape of the crystallites, the value of *k* ranges from 0.6366 to 1.5.[38] In the abscense of the detailed shape of the crystallites, as is the case here, the use of $k = 0.9$ is preferred.[39]–[41]

$$D = \frac{k\lambda}{B\cos\theta} \qquad \text{Equation 3}$$

2.6 Mechanical and Electrical Characterization of Origami structure

The structural density of the Miura-ori samples was calculated by the ratio between the mass of the Miura-ori and the total volume it occupied, i.e. the envelope method.[42][43] We performed compressive tests on the heat treated Miura-ori samples to characterize the compressive strength (σ_m) and the elastic modulus (E) of the samples. The compressive tests were performed at a rate of 1 mm/min to 80% strain using a load cell of 50 N mounted in a an Instron Single Column Testing System (Model 5944). The stress-strain curve obtained from the compressive test featured three different regions: the elastic region, post-yielding softening and densification.[44][45] A representative example of such stress-strain curve is presented as Figure S1 in the supplementary information. The highest peak in the elastic region determined the compressive strength (σ_m) reported here, which represents the onset of fracture of the panels, while the slope of the curve in the elastic region determined the elastic modulus of the sample (E).

To characterize the electrical stability of the heat-treated origami samples, LabView software was used with a National Instruments myDAQ to apply a constant current of 1mA through the test samples and measure the resistance during the compression tests. Electrically insulating rigid plates were used during the compression test to ensure no transfer of current from the testing samples to the test fixture occurred. Connections from the myDAQ to the sample were made by fastening a positive and negative lead to two bands of copper tape which were adhered to the lower insulating plate of the test fixture at a distance of 4.5 mm. Resistance measurements were recorded at a rate of 2 Hz. Figure S2 shows a picture of the experimental setup.

3. RESULTS AND DISCUSSION

3.1 WC Origami

The Miura-ori structures obtained after heat treatment appeared grey in color and although they shrunk, the Miura-ori shape was retained after heat treatment (Figure 1c). The Miura-ori structures featured a structural density in the range 0.06-0.11 g/cm^3, or 0.38-0.7% of an equivalent prism made of solid WC as measured by the envelope method.[46] The shrinkage of the Miura-ori occurs due to elimination of biproducts generated during the carbonization of the cellulose and the reduction of the AMT.[47][48] The shrinkage in the lateral direction of the Miura-ori was mostly attributed to the geometry of the Miura-ori as we explained in our recent publication regarding carbon origami.[49]

3.2 Heating rate during heat treatment is not as an important process parameter as AMT concentration and temperature in the fabrication of WC Origami

We studied the effect of heating temperature, heating rate and concentration of ammonium meta tungstate (AMT) solution on the composition of the heat-treated samples by using design of experiments, Taguchi method and Analysis of Variance (ANOVA) analysis. The amount of WC produced in the heat-treated sample was considered as the output signal here, as our goal was to obtain a sample with the highest purity of WC. The analysis obtained by ANOVA and the results from the Taguchi analysis are presented in Table 2 and Figure 2. The equations used to calculate the total square of sum (SS), mean square of a factor (MS), F-value and P-value can be found in previous publications.[50][51] Of particular interest is the F-value that indicates the effect of the control factor on the results obtained.[28] A F-value less than 1 indicates minimal effect of the control factor on the result; a F-value around 2 represents moderate influence of the control factor on the outcome; while A F-value more than 4 suggests strong and significant effect of the control factor. In the Taguchi analysis, the impact of a parameter on the output signal, such as the relative amount of WC of interest here, is analyzed by the slope of the curve,[28] i.e. a flat curve signifies minimal impact. Here, both the ANOVA and the Taguchi analysis strongly suggested that only temperature and AMT concentration had an impact on the final material, with temperature being slightly more important than AMT concentration. Furthermore, the analysis of the mean S/N ratio and the relative amount of the WC obtained from the Taguchi analysis suggested a synthesis temperature of 1300 °C (level 3), heating rate of 2.5 C/min (level 2) and AMT concentration of 10% (level 1) to be the ideal conditions among those tested. Further work was done to further elucidate the impact of temperature and concentration of AMT.

Table 2: ANOVA of the S/N ratios for the relative amount of WC depending on temperature and AMT. The descriptors for each Level are detailed in Table S1. A low F-value indicates weak impact. The highest value of mean S/N ratio indicates the most optimized value in the array.

Source	***DF***	***SS***	***MS***	***F- value***	***P- value***	***Mean S/N ratio***		
						Level 1	*Level 2*	*Level 3*
Temperature	2	75.08	37.54	17.61	0.054	28.19	48.59	**56.67**
Heating rate	2	3.16	1.58	0.74	0.574	43.26	**45.17**	45.02
AMT	2	82.99	41.49	19.46	0.049	**54.88**	53.12	25.46
Error	2	4.27	2.13					
Total	8	165.49						

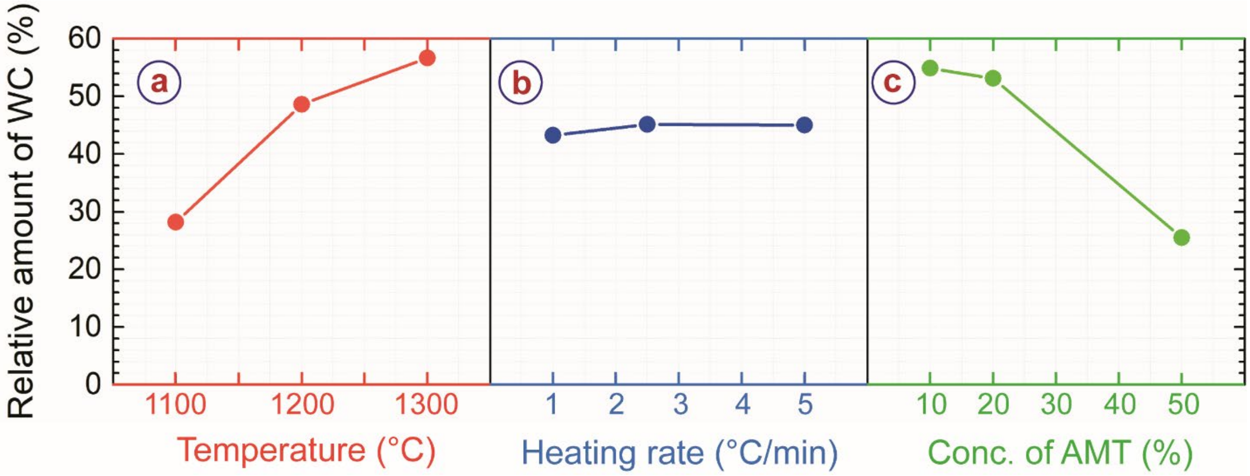

Figure 2: Effect of (a) temperature, (b) heating rate and (c) concentration of AMT on the synthesis of WC from paper obtained from the design of experiment using Taguchi analysis. This analysis is based on the crystalline phases obtained in the XRD patterns of the heat-treated sample as calculated using Equation 1.

3.3 Effect of AMT concentration

The amount of AMT can be used to alter the stoichiometry in the system – reduced amounts of AMT will yield an excess of amorphous carbon, while excess of AMT will yield an excess of tungsten. In the system studied here, carbon is first required for the carbothermal reduction of tungsten oxide to tungsten, and second for the reaction with W to generate WC. An ideal concentration of AMT should provide enough W that is in stoichiometry to the carbon derived from the paper and after the reduction of WO_3 to W. The molar ratio of W:C at stoichiometry is 1 for the formation of WC. We first studied the effect of AMT concentrations in the range 5% - 50% in our material system when assuming a carbon yield of 4.4% from the paper.[49] Figure 3a shows that a molar ratio W:C of 1 is achieved in this case when using an AMT concentration close to 30%. Of note, these calculations were obtained using a carbon yield percentage obtained in nitrogen atmosphere and not considering the carbon required for the reduction of WO_3. The use of a vacuum atmosphere is expected to result in a lower carbon yield than when using nitrogen as previously reported by Dickens when studying the carbonization of polyethylene in both atmospheres.[36] However, the exact value for the paper used here is not reported in the literature and we could not derive it due to equipment limitations. Hence, we expected the actual amount of carbon available for the reaction with the metallic W to be lower than the 4.4% originally assumed. To explore the effect of lower carbon yields, we then plotted the estimated molar ratio of W:C when the carbon yield is 2% and 3% (Figure 3a). This resulted in estimating that a ratio of 1 can be achieved at AMT concentration of 13% and 23% respectively.

We heat treated the infiltrated Miura-ori shapes to 1300 °C with a heating rate 2.5 °C/min to characterize the effect of the AMT concentration on WC synthesis. The results from XRD characterization (Figure 3b and c) indicate that a) AMT concentrations less than 10% lead to an excess of carbon; b) an AMT concentration 10-20% derives in a sample where WC seems dominant, with small peak for W_2C; and c) AMT concentrations ≥30% yield a clear excess of W, with WC present and no traces of W_2C. A closer inspection of the XRD patterns for the samples with 10% and 20% AMT revealed that a significant amount of carbon was still present as indicated by the bulging curve between $2\theta= 20°$ to $2\theta= 30°$ in the XRD pattern (Figure 3c). The best fit curve to the bulged portion seems very similar for both samples, so it is difficult to estimate which sample contains more carbon. However, the plot of the crystalline composition of the sample for different AMT concentrations (Figure 3d) shows that the relative amount of WC is 95.5% for 20% AMT compared to 87.35% for 10% AMT. Hence, it can be inferred that in the case of 20% AMT, more WC was formed, and more carbon was consumed to form WC. With further increase of the AMT concentration to 30% or above, the bulging curve for the amorphous carbon in the XRD pattern became flat, which suggests all the carbon was consumed to form WC. However, metallic W became the dominant material in the sample. Hence, the exact AMT concentration which satisfies the stoichiometry between carbon and tungsten is likely to be between 20%-30% and closer to 20% AMT as indicated by Figure 3d. This will mean that the available carbon for carbothermal reduction and WC synthesis in this system is around 3% of the paper as estimated by Figure 3a. This is corroborated by the fact that the intersect at W:C=1 for different carbon yields is inversely proportional to the AMT concentration.

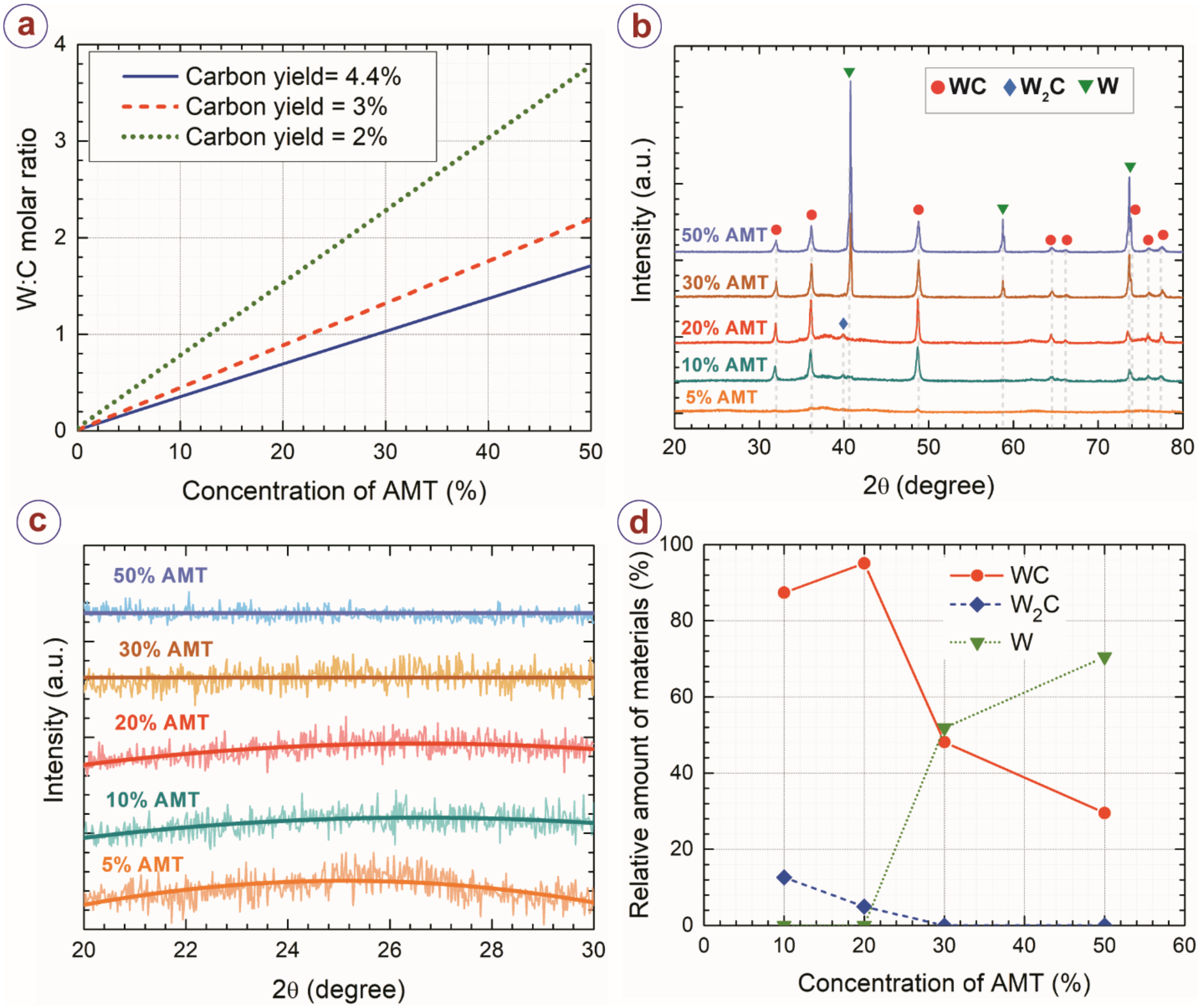

Figure 3: (a) Molar ratio between W and carbon estimated analytically based on the AMT absorbed by the cellulose paper during the infiltration. Different carbon yields of the paper were also considered here. (b) XRD patterns for the samples obtained using different concentration of AMT and heat treated at 1300ºC with a heating rate of 2.5ºC/min. The peaks for hexagonal tungsten carbide (WC) are identified at the 2θ angles of 31.7°, 35.9°, 48.6°, 64.4°, 66.1°, 73.5°, 75.8°, and 77.3° which are indexed to the (001), (100), (101), (110), (002), (111), (200) and (102) crystal planes respectively (ICDD PDF number 01-089-2727). The other major peaks in the XRD patterns are indexed to tungsten hemicarbide (W_2C) and tungsten (W) according to ICDD PDF numbers 01-071-6322 and 00-001-1204 respectively. (c) The XRD patterns zoomed in the range 2θ = 20° to 2θ = 30°, which is important to investigate the presence of any free carbon the sample. The samples for 5%, 10% and 20% AMT exhibit a bulging curve indicative of free carbon present in the samples. (d) Effect of the concentration of AMT on the relative amount of the crystalline

phase materials present in the samples heat-treated to 1300°C. The relative amount of the crystalline phase materials was calculated using Equation 1.

3.4 Effect of Synthesis Temperature

The XRD patterns of Miura-ori infiltrated with 20% AMT and heat-treated at 2.5°C/min to different temperatures in the range 800°C – 1300°C are shown in Figure 4a. The relative proportion of the crystalline materials present in the sample using the XRD patterns is plotted in Figure 4b as calculated with Equation 1. At 800°C, the peaks in the XRD pattern correspond to WO_3, confirming the known reduction of AMT into WO_3 at temperatures below 800°C.[52] As the temperature increased, WO_3 reduced to W followed by reaction with carbon to generate WC. The reduction of WO_3 to metallic W completed at a temperature in between 800°C – 900°C as evidenced by the wide peak around $2\theta = 40.3°$ at 900°C and the disappearance of the peaks at $2\theta = 23.94°$, 24.84° and 53.36°, which are characteristic peaks of WO_3. WC was not observed below 900°C. The presence of amorphous carbon in the system can be deducted by the bulge between the angles $2\theta = 20°$ to $2\theta = 30°$ in the XRD spectra. At 1000°C, peaks for WC and W_2C appear but metallic W is still the dominant material in the sample. The relative amount of WC increases proportionately with temperature until becoming the dominant phase around 1200°C. At 1300°C, the relative amount of W becomes zero, which suggests complete carburization of the metallic W. Although the amount of W_2C decreases with temperature, a small amount of W_2C is still present in the sample obtained at 1300°C. At this temperature, the amount of WC is 96% and the rest of 4% is W_2C. We expect the W_2C to completely carburize to WC by heating above 1400°C based on previous report by Koc and Kodambaka when heat treating carbon coated WO_3 powders in a argon (Ar) or 10% H_2-Ar atmosphere.[53] We could not do test at a temperature higher than 1300°C due to limitations of the experimental set up.

The field emission scanning electron microscopy (FESEM) images of the samples heat treated at a temperature 1000°C – 1300°C are shown in Figure 4c–f. The FESEM images support the results from the XRD patterns. For the samples heat treated at 1000°C and 1100°C, a significant amount of W particles can be seen in their corresponding FESEM images (Figure 4c and 4d respectively). For the sample obtained at 1000°C, the W particles were sitting on the carbon fiber template. Example of such is presented in the inset of Figure 4c. As the temperature increased to 1100°C, the W particles seemed to start arranging themselves along the fibers, although a significant number of particles were still sitting on the fibers. The size of the W particles also seemed bigger than the one seen in the sample of 1000°C. In the FESEM images for 1200°C and 1300°C, the loose W particles were not seen anymore. However, there were still W particles present in the sample obtained at 1200°C as the XRD suggested. These W particles might be embedded in the inner part of the fibers, which are not visible in the FESEM images. Fibers composed of agglomerated WC particles can be seen for the sample obtained at 1300°C. Details of the microstructures of this sample are discussed in a later section.

We investigated the effect of synthesis temperature on the specific surface area and pore size distribution of the samples. The results are shown for the samples heat treated at 900°C, 1100°C and 1300°C in Figure 5. As shown in Figure 5a, all the samples exhibited type I adsorption-desorption isotherms, which are classified according to international union of pure and applied chemistry (IUPAC).[54] The adsorption-desorption isotherms suggest presence of mesopores (pore diameter = 2-50 nm) in the samples, which was further confirmed by the pore size distribution as shown in Figure 5b. Along with the mesopores, presence of internal macropores (pore diameter > 50 nm) can be also confirmed from the pore size distribution for all the samples. The porosity parameters of the samples are summarized in Table 3. The BET surface area, total pore volume and mesopore volume decreased with the increase in the synthesis temperature. This was expected as increase in synthesis temperature promotes sintering of the particles, which results in collapsing the pores and formation of larger particles. Consequently, these yields lower specific surface area and pore volume.

Both the XRD and the FESEM analysis suggest that the carburization process implemented here completed at 1300°C. This is a lower temperature than those required in traditional WC synthesis methods such as high temperature direct carburization, carbothermal reduction reaction and gas phase carburization. For example, the high temperature direct carburization requires a temperature around 2800°C for fusion of tungsten and carbon in a hydrogen environment.[55] Both carbothermal reduction reaction and gas phase carburization require a temperature in the range 1400°C–1800°C for complete carburization of tungsten.[56] We speculate that the infiltration of the AMT within the cellulose help the WO_3 particles nucleate inside a carbon matrix. The close proximity between the carbon and the WO_3 particles might accelerate the whole reaction mechanism yielding a lower carburization temperature. Since lower carburization temperature signifies lower energy consumption, our process is a more energy-efficient process compared to traditional WC synthesis processes. However, a temperature of 900°C–1000°C has also been previously reported when using AMT as a tungsten precursor.[6][57]–[59] In these reports, a sol-gel method was used to prepare the precursor material. In a sol-gel method, the AMT is surrounded by the gel material, which helps the nucleation of the tungsten particle and initiation of the carburization at lower temperature. Furthermore, preparation of the gel requires a heat treatment at a temperature 180°C–200°C for at least 12 hours. We suspect this intermediate heat treatment process may already weaken the W–O bonds of AMT, which further helps the carburization to occur at a lower temperature. In our process, such long intermediate heat treatment is missing. Furthermore, we suspect that because of the amorphous and non-graphitizable nature of the carbon, the process needs higher energy than the sol-gel process to facilitate complete carburization of the W particles, which is facilitated by an increase in temperature. However, it should be noted here that the samples we obtained in our process feature a minimum specific surface area of 102.06 m^2/g. This is significant because such surface area is much higher than the surface area of commercial grade WC (BET surface area < 10 m^2/g) obtained using carbon black and tungsten precursors.[60] WC featuring higher porosity and BET surface area (>100 m^2/g) can be synthesized using template methods.[61][62] In such method, a sacrificial material is used in the matrix to generate the pores. Removal of the sacrificial material generally requires a washing step with highly corrosive chemical such hydrofluoric acid. Use of the highly selective sacrificial materials and precautions taken for the highly corrosive chemicals yields higher processing cost for the template method. In comparison, we were able to achieve a surface area >100 m^2/g for the WC in a simple, cost-effective and environment-friendly process.

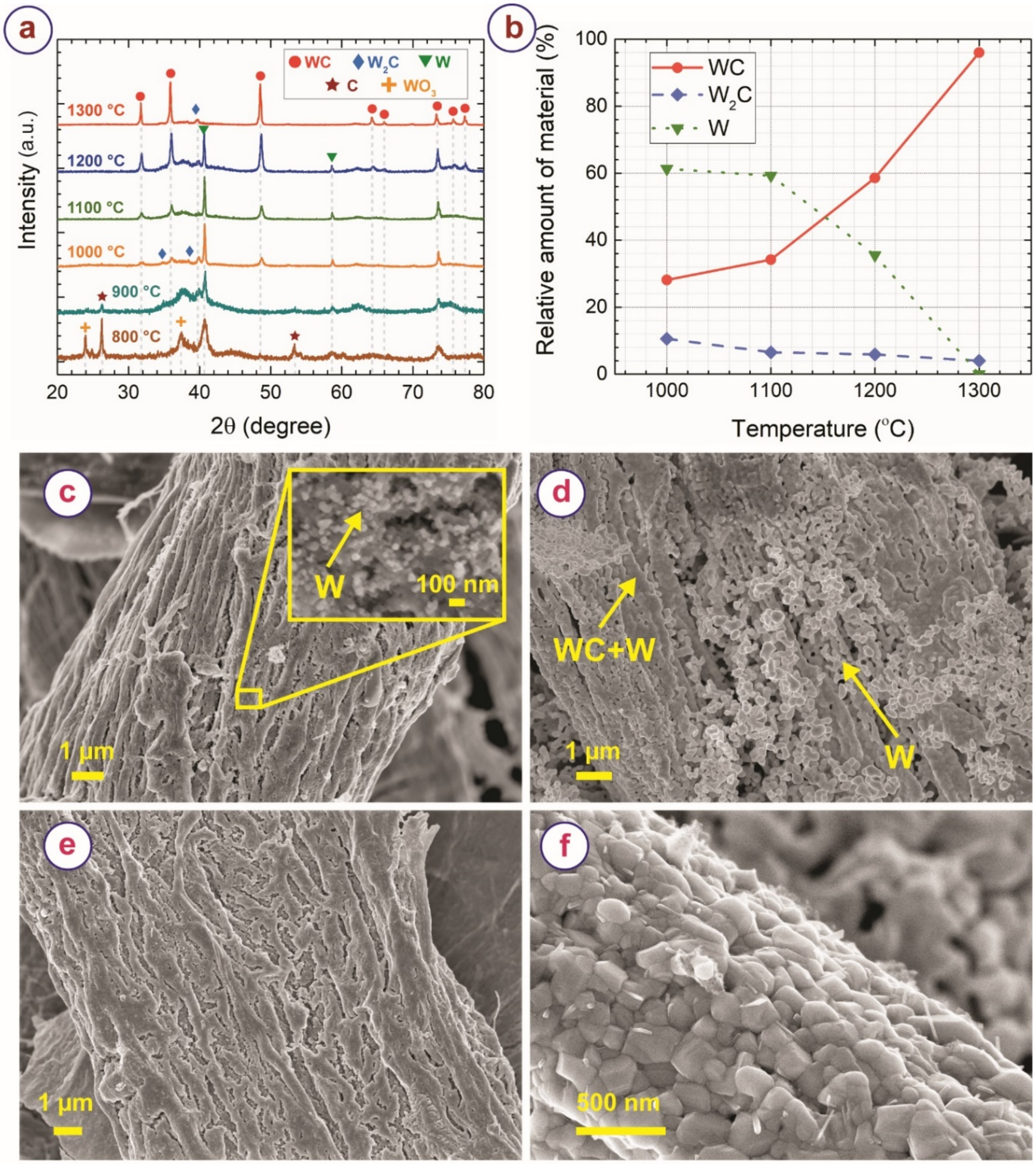

Figure 4: (a) XRD patterns for the heat-treated Miura-ori samples at different temperature and both constant heating rate (2.5°C/min) and AMT concentration (20%). (b) Relative amount of the crystalline materials present in the heat-treated Miura-ori samples at different temperature. The relative amount was calculated from the XRD patterns using the Equation 3. FESEM images of the samples heat treated at (c) 1000°C, (d) 1100°C, (e) 1200°C and (f) 1300°C. For the sample obtained at 1000°C, tungsten particles were sitting on carbon template as seen in the higher magnification FESEM images. Example of such is shown in the inset of (c).

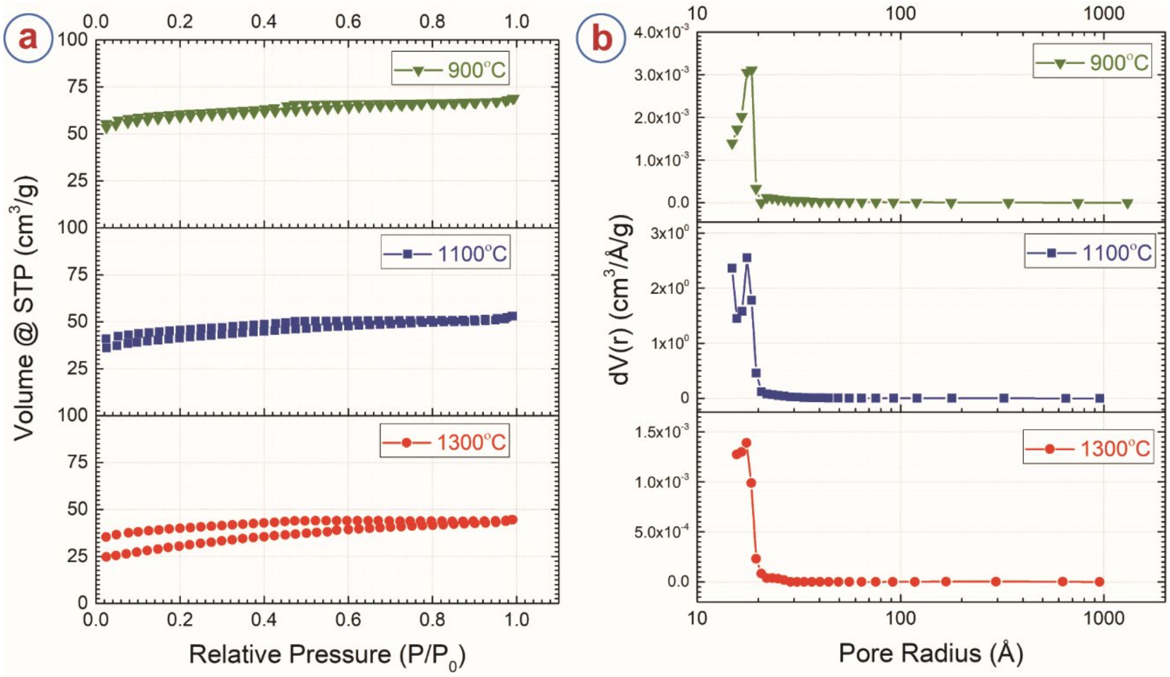

Figure 5: (a) Nitrogen adsorption-desorption isotherm at 77.35K and (b) pore size distributions of the samples heat treated at 900°C, 1100°C, and 1300°C.

Table 3: BET surface area and pore volume of the samples heat treated at 900°C, 1100°C, and 1300°C.

Synthesis temperature	**BET surface area (m^2/g)**	**Total pore volume (cm^3/g)**	**Mesopore volume (cm^3/g)**
900°C	181.96	0.303	0.070
1100°C	130.22	0.224	0.052
1300°C	102.06	0.129	0.032

3.5 Microstructural characterization

The microstructure was characterized for the Miura-ori obtained using a temperature of 1300°C, a heating rate of 2.5°C/min and 20% AMT since previous experiments determined that WC was the dominant material in this case. The paper used in this work as carbon precursor was basically a multilayered porous matrix of tightly packed cellulose fibers with an average diameter of 17.48 ± 3.06 µm.[49] After heat treatment, the spacing between fibers was still random with macroporosity of the sample in the range from 1.04 µm to 28.34 µm (inset of 6a). Interestingly, the microstructure of the fibril network on the outer layer was different from that in the inner layer. The average diameter of fibers forming the outer layer was 10.88 ± 2.05 µm, whereas the fibers in the inner layers featured an average diameter of 15.62 ± 1.73 µm. Higher magnification FESEM images further showed that the fibers on the outer layer were composed of what seemed to be homogeneous grains (Figure 6b). TEM studies showed how the WC grains at the outer layers featured a lattice spacing (*d*) of 2.5Å (Figure 6d), which corresponds to the (100) plane of hexagonal WC.[63] On the contrary, the inner-layer fibers appeared to be amorphous carbon decorated with solid particles (Figure 6c), which was further confirmed by the TEM as shown in Figure 6e. Using the EDS analysis (inset of Figure 6c) of the inner-layer, the weight ratio between WC and carbon in the inner layer fibers was estimated to be 2.59 ±0.39.

The initial hypothesis to explain such inhomogeneity in the sample was an inhomogeneous infiltration of the AMT solution across the cross-section of the paper. To test this hypothesis, we infiltrated the paper with a colored AMT solution (using food coloring at 10 v/v%). However, this hypothesis was ruled out after a homogenous color across the cross-section of the AMT infiltrated paper was observed under the microscope. The effect of dwell time and temperature was then considered, following the rationale that the reaction between W and C throughout the sample was incomplete at 1300°C. However, XRD results showed how at 1300°C there was no W left in the system to react with the carbon. Our current hypothesis is that the evaporation of water occurring after AMT infiltration may be the cause for material inhomogeneity. During evaporation, water may aid on the transport of AMT to the outer layer and the correspondent depletion of AMT in the inner layers. Moreover, the reduction of AMT begins with the decomposition of AMT to WO_3, gaseous ammonia (NH_3) and water (H_2O),[52] which is followed by the reaction between H_2O with WO_3 to form $WO_2(OH)_2$, a volatile byproduct,[47] that may get redeposited on the outer layer fibers. Both processes can lead to a change in stoichiometry and material inhomogeneities across the material and further investigation is needed.

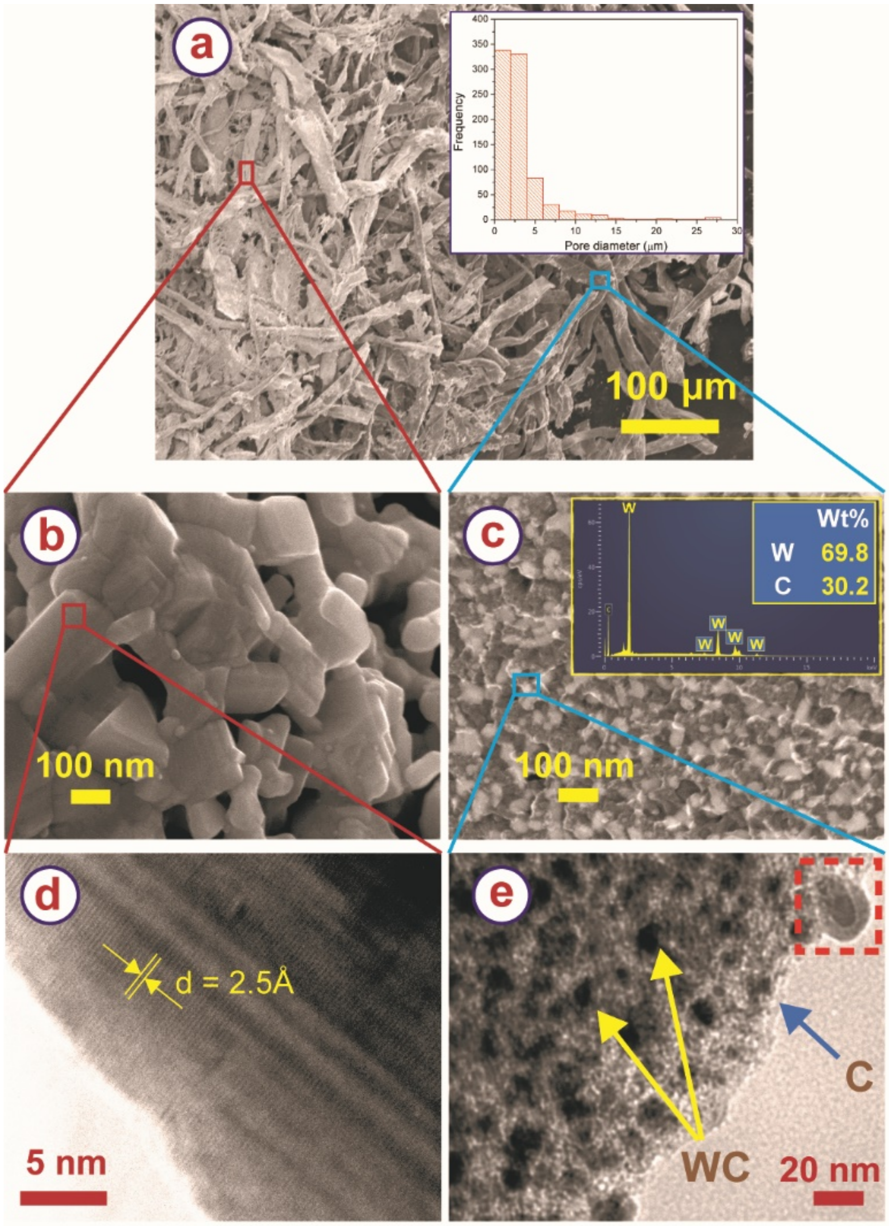

Figure 6: (a) FESEM image of the sample obtained from the heat treatment of paper at a synthesis temperature of 1300°C with a heating rate of 2.5°C/min and using an AMT concentration of 20%. The WC obtained here featured a porous network of randomly oriented fibers. The pore size distribution of the fibers is shown in the inset. The pore size between the fibers ranged from 1.04 μm to 28.34 μm. The microstructure of the fibers from outer layer of paper differed from the fibers from the inner layer. (b) Higher magnification FESEM image of the fibers from the outer layer showing the porous network of agglomerated WC particles. (d) HRTEM image of these WC particles shows the lattice planes of WC with a lattice spacing of 2.5 Å. (c) Higher magnification FESEM image of the fibers from the inner layer of the sample showing WC decorated in a carbon

matrix. A representative EDS result of the inner layer fibers is shown in the inset. (e) HRTEM image of the inner layer fiber further confirms this phenomenon showing WC particles surrounded by carbon.

3.6 Mechanical Characterization of WC Miura-ori

We characterized the compressive and elastic modulus for the Miura-ori samples heat treated in the temperature range 900°C – 1300°C. The results are reported in Figure 7c. The decrease of -68.76 ± 0.17% in the compressive strength and -59.06 ± 0.22% in the elastic modulus were not expected given that WC gradually becomes the dominant material in the sample in this temperature range. The high standard deviation in both compressive strength and elastic modulus was expected due to the random distribution of the constituent fibers characteristic of paper.[49] The decrease in the mechanical properties was not due to structural density as this remained uniform (Figure S3) but can be attributed to the properties of the constituent materials, namely WC, W, W_2C and amorphous carbon. According to the Hall-Petch relation, the mechanical properties of ceramics decrease with the increase in the grain size as long as the grain size of the ceramic is larger than 15 nm.[64][65] The grain size of WC and W present in the material at different temperatures is shown in Figure 7a; the contribution of W_2C was insignificant and is not reported here. The grain size of WC increased from 16.1 ± 8.63 nm at 1000°C to 58.88 ± 5.81 nm at 1300°C while that of metallic W increased from 26.94 ± 3.52 nm at 900°C to 67.3 ± 2.19 nm at 1200°C. Furthermore, the mechanical properties of amorphous carbon also decrease with increasing temperature.[66][67] In addition to that, at the interface of the crystalline phase materials (WC or W) and carbon, the carbon is expected to locally transform into graphitic phases with increasing temperature.[68][69] The graphitic phase carbon exhibit lower mechanical properties than the disordered carbon. As a result, cracks may appear at the interface of the carbon and crystalline phase material during load transfer, which would further propagate along the fibers to cause brittle fracture of the fibers.[70] As the local graphitization enhances with increasing temperature, failure at a lower stress is expected at a higher temperature. Therefore, the overall mechanical properties of the Miura-ori structures exhibited an inversely proportional relation with the temperature. It should be noted here that we obtained a range of compressive strength and elastic modulus only by changing the process temperature of the Miura-ori and without changing the density of the structure. When using the system detailed here, a lower synthesis temperature should be chosen when the mechanical properties are the most important, even if a pure WC is not obtained at that temperature. Further investigation is required to identify the reagents and process necessary to derive pure WC with small grain size.

3.7 Electrical Characterization of WC Miura-ori

Without any mechanical load, the resistance of WC origami ranged from 44.5 ± 28.91 Ω when derived from a heat treatment at 900°C to 18.5 ± 6.37 Ω at 1300°C, thus showing an inversely proportional relation between electrical resistance and processing temperature. This can be attributed to the change in material composition with the increase in temperature. At 900°C, the composition of the material is mostly W particles in a carbon matrix as suggested by the XRD (Figure 4a). Although W features low electrical resistivity (6.01 μΩ·cm)[71], that of carbon derived from cellulose is much higher than W (300 – 500 μΩ·cm).[72] As the temperature increases, W particles start reacting with the surrounding carbon to produce WC, which features low electrical resistivity (4.2 – 100 μΩ·cm).[14] The resistivity of the carbon is also known to decrease with increasing processing temperature.[73] Furthermore, local graphitization at the interface of the W/WC and carbon can also induce higher conductivity at a higher processing temperature, as the catalytic graphitization is strongly influenced by temperature.[69] An example of this is shown in the detail (red dashed square) in Figure 7e for a sample heat treated at 1300 °C.

We then characterized the electrical stability of the heat-treated origami samples under mechanical stress. A representative example of the electrical behavior of the Miura-ori sample under compression test is shown in Figure 6b, where we plotted the electrical resistance and the stress-strain curve of the corresponding sample (in this specific case the sample was heat treated at 1300°C). The initial resistance drops from a strain of 0 to ~0.26 represents the decrease in contact resistance between the sample and the measurement electrodes (labeled as contact resistance in Figure 6b). Once the mechanical load is transferred to the sample, the electrical resistance remains constant up to the point of structural failure (elastic region). The measured resistance then increased slightly after failure (post-yield softening). The point of failure when under compression and its corresponding resistance as the processing temperature changes are plotted in Figure. 7d. We speculate that under compression the inter-fibril contacts increase and the relative distance among the fibers decreases, which improves the electron transport and decreases the electrical resistance. As the load increases, the stress would ultimately transfer from fiber-fiber contacts to the suspending portion of the individual fibers. At the onset of the post-yield softening, the fibers start rapturing progressively, ultimately leading to structural failure and an increase in the electrical resistance of the sample in the post-yielding softening region. The average electrical resistance of the samples heat-treated at different temperature is plotted in the Figure 6d when subjected to no load and at the compressive strength immediately before failure. Electrical resistance clearly decreases with increasing processing temperatures. Importantly, the Miura-ori samples remained electrically conductive throughout the compression test up to mechanical failure. The small standard deviation for the data taken under the compression suggests the electrical conductivity of the origami samples was stable during the compression test. Such behavior is highly desirable from architected electrode materials.

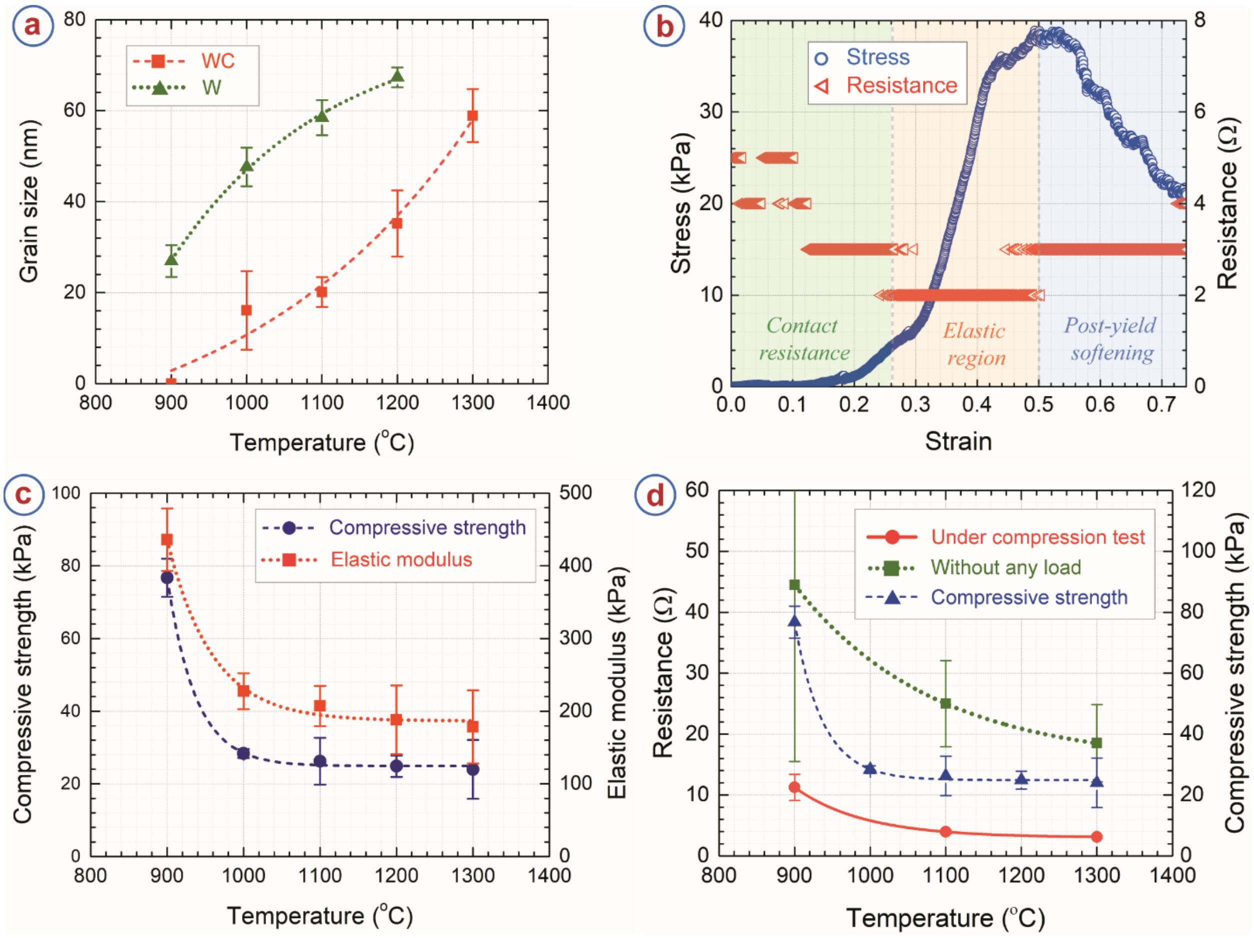

Figure 7: (a) Effect of synthesis temperature on the grain size of WC and W. The grain size was estimated from the XRD patterns using Scherrer equation. (b) Representative example of the stress-strain curve and corresponding electrical resistance of a heat-treated Miura-ori sample obtained during compression testing. Three distinct regions of the curve can be identified: contact resistance, elastic region and post-yield softening. This specific sample was heat treated at 1300°C. (c) Compressive strength and elastic modulus of the Miura-ori samples heat-treated at different temperature. (d) Electrical resistance of the Miura-ori samples heat treated at different temperature when under no load (squares) and at the compressive strength immediately before failure (circles). The compressive strength of the Miura-ori samples is also plotted here to corelate the mechanical properties and the electrical properties of the samples. The Miura-ori samples were infiltrated with 20% AMT solution. The heat treatment was performed in vacuum environment using a heating rate of 2.5 °C/min. At least 4 experiments were performed for each data point. The error bar represents the standard deviation in the measurement.

3.8 Scalability and Versatility

The fabrication process presented here is scalable and versatile. The size of the origami structures can be scaled up or down by changing the dimensions in the unit cell. For example, the scalability for WC Miura-ori is shown in Figure 8a, where the unit cell parameter h was varied from 6.12 mm to 10.71 mm and the design angle α was kept constant at 75º. Examples of other shapes of WC origami and their corresponding unit cell geometries are shown in Figure 8d and e in the forms of Waterbomb-base and Yoshimura. The scalability of the WC origami structures is dependent on the fabrication of the paper origami shapes, as reported recently for the case of carbon origami.[49] When using a manual folding approach, scalability depends on the dexterity of the user and complexity of the origami structure. Hence, if the complexity of an origami structure is defined by N, which is a ratio between the number of crease lines and the area of the paper, scalability is inversely proportional to N. An $N > 0.05$ mm^{-2} makes the distance between adjacent crease lines for the origami structures too close for manual folding by an average user. In such cases, folding defects such as curl, crimps and kinks occur at the facets of the paper structure during the manual folding and are transferred further in the WC origami structures (data not shown). The scalability of the fabrication process could be improved by replacing the manual folding step with reprogrammable robotic systems. For example, Tanaka et al built a robotic mechanism that could be programmed to mimic human hand dexterity for origami folding, which was demonstrated by successfully folding a flat piece of paper into an origami tadpole.[74] Furthermore, Namiki and Yokosowa developed a dynamic sensory system for a robotic arm that could help avoid the occurrence of defects in successive folding and improve folding accuracy.[75]

The structural density and mechanical properties vary with the scalability of the WC Origami structures. Figure 8b shows the change of structural density (ρ) for WC Miura-ori structures with different design parameter h. The density of the WC Miura-ori decreases from 0.108 ± 0.015 g/cm^3 to 0.052 ± 0.006 g/cm^3 as h increases from 6.12 mm to 10.71 mm. Such change in density with the size can be attributed to the shrinkage of the origami structures during the heat treatment process, which is further associated to the geometrical parameters of the origami shapes.[49] Figure 8c shows the compressive strength (σ_m) and the elastic modulus (E) of the WC Miura-ori samples. As expected, σ_m and E increase with the increase in the structural density. The value of σ_m increases from 16.68 ± 4.95 kPa for $\rho = 0.052$ g/cm^3 to 39.48 ± 5.8 kPa for $\rho = 0.108$ g/cm^3. Similarly, E increases from 118.18 ± 20.14 kPa to 265.09 ± 35.8 kPa. In other words, σ_m and E show an inverse relationship with the design parameter h. Such structural behavior is also valid for other WC origami shapes such as Waterbomb-base and Yoshimura. The structural density and mechanical properties of the origami shapes are also supposed to vary with the shape of the origami structure.[76] Such variation of the structural properties can be an advantageous aspect of this fabrication process. It helps to choose the geometrical dimensions of the electrodes depending on the application specific working conditions. For example, electrodes in fuel cells for automobiles are subjected to several mechanical stresses including packaging stress and vibrational stress.[77] For such application, origami structures exhibiting higher mechanical properties and higher density may be suitable.

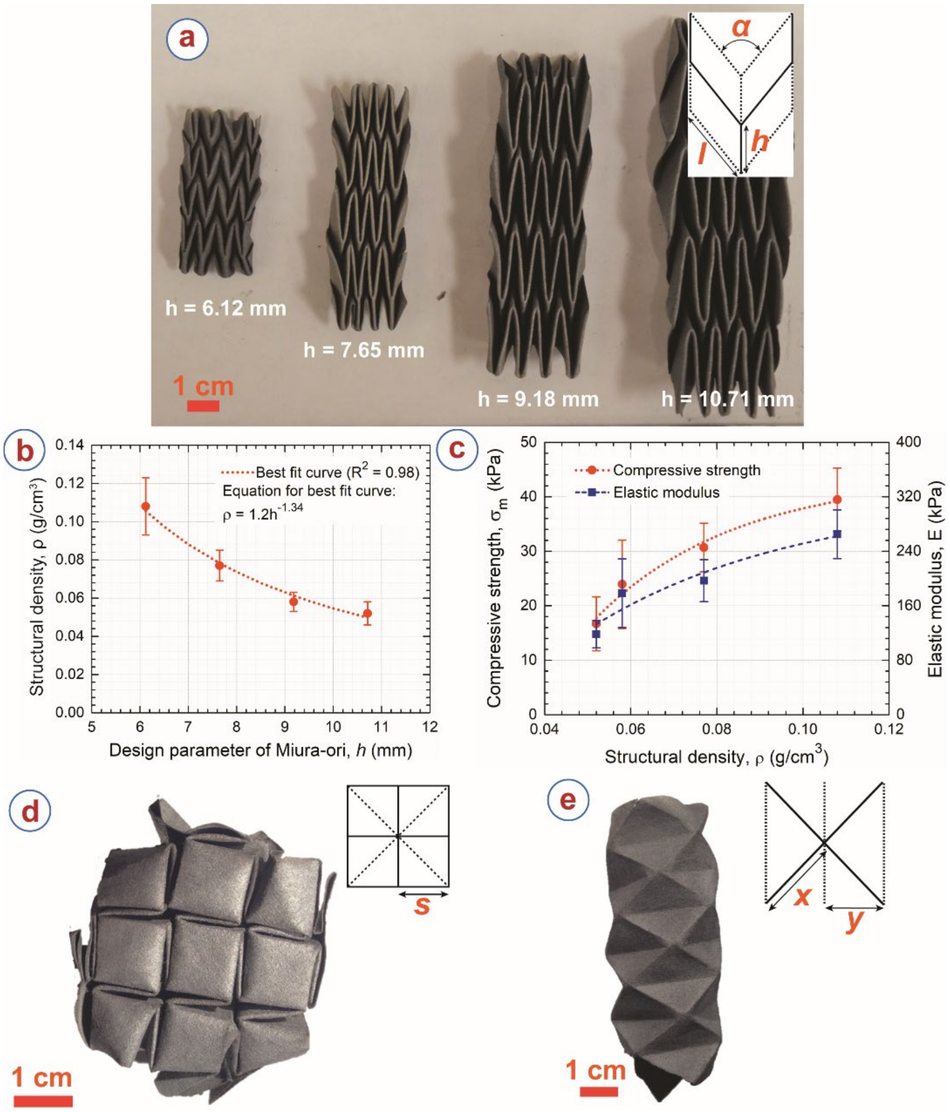

Figure 8: (a) Different sizes of WC Miura-ori with varying *h* from 6.12 mm to 10.71 mm showing scalability of the fabrication process. (b) Structural density (ρ) of the WC Miura-ori structures of different sizes. At least five Miura-ori were characterized for the structural density for each value of *h*. The error bars represent the standard deviation in the measurement. The red dotted line represents the best fitted curve to the density. (c) Plots of compressive strength (σ_m) and elastic modulus (E) against structural density of the WC Miura-ori. Different other shapes of WC can be fabricated using this origami-inspired manufacturing. Examples are (d) WC Waterbomb-base and (e) WC Yoshimura. The unit cells with the geometrical parameters are shown in the inset of the corresponding figures.

4. CONCLUDING REMARKS

In this work, we elucidated the effect of heating rate, AMT concentration and temperature on the composition of WC structures. Heating rate was found to not have a significant impact on the material composition. A low AMT concentration resulted in amorphous carbon being the main component of the structure, whereas an excess of AMT yielded a structure rich in tungsten. The synthesis temperature influences the reaction between W and C, yielding higher purity of WC with increasing temperature. Although the focus was first on deriving pure WC, increasing the purity of WC decreased the mechanical properties of the origami structure. This can be attributed to the increasing grain size of the crystalline phase materials and increase of graphitic phases in carbon with increasing temperature. The electrical conductivity of the heat-treated origami samples also decreased with increasing purity of WC, which was expected. This is due to the conversion of the less conductive carbon into conductive WC, and a higher degree of graphitization of carbon with increasing temperature. The highest purity of WC, 96%, was achieved here at a synthesis temperature of 1300°C with a heating rate of 2.5°C/min and with an AMT concertation of 20%. The WC obtained using these synthesis conditions featured a BET surface area of 102.06 m^2/g, which is much higher than the surface area of commercially synthesized WC and comparable to the high surface area WC materials synthesized using template method. The WC Miura-ori samples exhibited good and stable electrical conductivity under compression, which is crucial for an architected electrode material.

The process to fabricate structured WC electrodes presented here can allow for the fabrication of unique geometries of porous, lightweight WC structures, which are challenging to achieve with other manufacturing techniques, including sintering, machining and additive manufacturing. The presented process also has potential for large scale manufacturing. For example, starting with a paper roll, automatic pre-creasing can be enabled with embossing techniques.[78]–[80] Upon pre-creasing, the paper roll can be passed through a bath of proper metal precursor for infiltration. The automatic folding of the origami structures can be implemented by using upcoming reprogrammable robots [74][75][81] or by the processes similar to the manufacturing of paper bags and filters.[82] The folded structures can be further heat treated using proper heating protocol on rolling furnaces, which are commonly used for manufacturing of tiles and other ceramic parts.[83] Lastly, it represents the use of sustainable precursors.

The results presented here encourage the use of paper as a scaffold to derive structures with various compositions, i.e. homogeneous carbide or carbon decorated with tungsten, for various applications. WC nanoparticles dispersed in a carbon matrix have been shown to exhibit excellent catalytic activity for hydrogen evolution reaction.[27][84] Carbon-coated WC fibers obtained by heat treatment of electrospun AMT-infiltrated polyvinylpyrrolidone fibers exhibited preferable electrocatalytic activities and stabilities in oxygen reduction reaction.[85] Although the WC fibers obtained in the work presented here feature larger diameters than the electrospun WC fibers, comparable electrochemical activities can be expected from our materials due to compositional similarity and fibril morphology. In addition to that, the origami pattern imposes an impact on the electrochemical properties by increasing the energy per footprint area, which is beneficial for energy devices. For example, Cheng et al. reported an 14-fold increase in areal energy density for a Miura-ori patterned current collector when compared to a unfolded current collector in a Lithium-ion battery application.[86] Furthermore, we demonstrated that these origami structures of WC feature low density, can carry mechanical loads at such low density and exhibits good and stable electrical conductivity under compressive load. Hence, complementing the excellent electrochemical properties of the WC materials reported by other authors with the load carrying capabilities and electrical stability of the WC origami structures, the fabrication process presented here can be suitable to fabricate multifunctional materials for structural energy devices. Ongoing work is on the validation of the multifunctionalities of these WC origami structures by performing the electrochemical characterization under mechanical loading.

ACKNOWLEDGEMENTS

The authors acknowledge support from the Creative Inquiry program at Clemson University. Monsur Islam acknowledges financial support from Hitachi through a High Technologies Fellowship. The authors are thankful to several colleagues at Clemson University: Dr. Taghi Darroudi from the Electron Microscopy (EM) Laboratory for his advice during image acquisition; Dr. Laxmikant Saraf also from EM lab for his support of this work; and to the SCBioCRAFT Bioengineering and Bioimaging Core for facilitating the mechanical testing and measurement of electrical properties. The mechanical and electricals tests at SCBioCRAFT was supported by grant from National Institute of General Medical Sciences (*NIGMS)* of the National Institutes of Health (NIH) under award number 5P20GM103444-07.

CONFLICT OF INTEREST

The authors declare no conflict of interest

REFERENCES

[1] R.B. Levy, M. Boudart, *Science (80-.).* **1973**, *181*, 547.

[2] F. Harnisch, G. Sievers, U. Schro, *Appl. Catal. B Environ.* **2009**, *89*, 455.

[3] M.C. Weidman, D. V. Esposito, Y.C. Hsu, J.G. Chen, *J. Power Sources* **2012**, *202*, 11.

[4] Y. Liu, T.G. Kelly, J.G. Chen, W.E. Mustain, *ACS Catal.* **2013**, *3*, 1184.

[5] X. Yang, Y.C. Kimmel, J. Fu, B.E. Koel, J.G. Chen, *ACS Catal.* **2012**, *2*, 765.

[6] Z. Yan, M. Cai, P.K. Shen, *Sci. Rep.* **2013**, *3*, 1.

[7] M. Rosenbaum, F. Zhao, M. Quaas, H. Wulff, U. Schröder, F. Scholz, *Appl. Catal. B Environ.* **2007**, *74*, 261.

[8] X.G. Yang, C.Y. Wang, *Appl. Phys. Lett.* **2005**, *86*, 1.

[9] Y. Zhong, X.H. Xia, F. Shi, J.Y. Zhan, J.P. Tu, H.J. Fan, *Adv. Sci.* **2015**, *3*.

[10] P. Li, Z. Liu, L. Cui, F. Zhai, Q. Wan, Z. Li, Z.Z. Fang, A.A. Volinsky, X. Qu, *Int. J. Hydrogen Energy* **2014**, *39*, 10911.

[11] B.S. Koo, J.K. Lee, W.Y. Yoon, *Jpn. J. Appl. Phys.* **2015**, *54*.

[12] M. Rosenbaum, F. Zhao, U. Schröder, F. Scholz, *Angew. Chemie - Int. Ed.* **2006**, *45*, 6658.

[13] General Carbide, **2015**, 59.

[14] AZOMaterials, **2002**.

[15] M.F. Ashby, in *CES EduPack Resour. Bookl. 2*, **2010**, 1.

[16] L.E. Asp, E.S. Greenhalgh, *Compos. Sci. Technol.* **2014**, *101*, 41.

[17] T. Pereira, Zhanhu Guo, S. Nieh, J. Arias, H.T. Hahn, *J. Compos. Mater.* **2009**, *43*, 549.

[18] R.F. Gibson, *Compos. Struct.* **2010**, *92*, 2793.

[19] J. Wismans, E.-M. Malmek, J. Welinder, Y. Håland, M. Oldenbo, *Proc. 22nd Int. Tech. Conf. 'Enhanced Saf. Veh.* **2011**, 11.

[20] D.J. O'Brien, D.M. Baechle, E.D. Wetzel, *J. Compos. Mater.* **2011**, *45*, 2797.

[21] Z.Z. Fang, X. Wang, T. Ryu, K.S. Hwang, H.Y. Sohn, *Int. J. Refract. Met. Hard Mater.* **2009**, *27*, 288.

[22] M.W.R. Holgate, T. Schoberl, S.R. Hall, *J. Sol-Gel Sci. Technol.* **2008**, *49*, 145.

[23] S. Li, H. Fang, S. Sadeghi, P. Bhovad, K.W. Wang, *Adv. Mater.* **2019**, *31*, 1.

[24] C.D. Santangelo, T. Hull, R.C. Hayward, A.A. Evans, J.L. Silverberg, I. Cohen, L. McLeod, *Science (80-.).* **2014**, *345*, 647.

[25] K. Bertoldi, G.M. Whitesides, J.C. Weaver, Y. Shevchenko, S.A. Becerra, T.A. de Jong, J.T.B. Overvelde, C. Hoberman, *Nat. Commun.* **2016**, *7*, 1.

[26] C. Lv, D. Krishnaraju, G. Konjevod, H. Yu, H. Jiang, *Sci. Rep.* **2014**, *4*.

[27] C. Liu, J. Zhou, Y. Xiao, L. Yang, D. Yang, D. Zhou, *Int. J. Hydrogen Energy* **2017**, *42*, 29781.

[28] E.D. Kirby, *Technol. Interface* **2006**, *Fall*, 1.

[29] A. Kundu, B. Sen Gupta, M.A. Hashim, G. Redzwan, *J. Clean. Prod.* **2015**, *105*, 420.

[30] K.C. Cheung, T. Tachi, S. Calisch, K. Miura, *Smart Mater. Struct.* **2014**, *23*, 094012.

[31] C. Lv, D. Krishnaraju, G. Konjevod, H. Yu, H. Jiang, *Sci. Rep.* **2014**, *4*, 5979.

[32] R. Martinez-Duarte, P. Renaud, M. Madou, *Electrophoresis* **2011**, *32*, 2385.

[33] M. Islam, R. Natu, M.F. Larraga-Martinez, R. Martinez-Duarte, *Biomicrofluidics* **2016**, *10*.

[34] M. Islam, R. Martinez-Duarte, *Ceram. Int.* **2017**, *43*, 10546.

[35] J.B. Joo, J.S. Kim, P. Kim, J. Yi, *Mater. Lett.* **2008**, *62*, 3497.

[36] B. Dickens, *J. Polym. Sci. Polym. Chem. Ed.* **1982**, *20*, 1065.

[37] A.L. Patterson, *Phys. Rev.* **1939**, *56*, 978.

[38] J.I. Langford, A.J.C. Wilson, *J. Appl. Crystallogr.* **1978**, *11*, 102.

[39] U. Holzwarth, N. Gibson, *Nat. Nanotechnol.* **2011**, *6*, 534.

[40] V. Uvarov, I. Popov, *Mater. Charact.* **2007**, *58*, 883.

[41] L. Wang, *Aging Clin. Exp. Res.* **2018**, *2012*, 1.

[42] M.A. Worsley, S.O. Kucheyev, J.H. Satcher, A. V. Hamza, T.F. Baumann, *Appl. Phys. Lett.* **2009**, *94*, 1.

[43] S.M. Manocha, K. Patel, L.M. Manocha, *Indian J. Eng. Mater. Sci.* **2010**, *17*, 338.

[44] S. Callcut, J.C. Knowles, *J. Mater. Sci. Mater. Med.* **2002**, *13*, 485.

[45] A. Celzard, W. Zhao, A. Pizzi, V. Fierro, *Mater. Sci. Eng. A* **2010**, *527*, 4438.

[46] M.A. Worsley, S.O. Kucheyev, J.H. Satcher, A. V. Hamza, T.F. Baumann, *Appl. Phys. Lett.* **2009**, *94*, 1.

[47] C. Ma, N. Brandon, G. Li, *J. Phys. Chem. C* **2007**, *111*, 9504.

[48] K. Kong, L. Deng, I.A. Kinloch, R.J. Young, S.J. Eichhorn, *J. Mater. Sci.* **2012**, *47*, 5402.

[49] M. Islam, J. Flach, R. Martinez-Duarte, *Carbon N. Y.* **2018**, *133*, 140.

[50] M. Alfaresi, S. Yusup, *J. Appl. Sci.* **2010**, *10*, 3264.

[51] N. Raghunath, P.M. Pandey, *Int. J. Mach. Tools Manuf.* **2007**, *47*, 985.

[52] D. Hunyadi, I. Sajo, I.M. Szilagyi, *J. Therm. Anal. Calorim.* **2014**, *116*, 329.

[53] R. Koc, S.K. Kodambaka, *J. Eur. Ceram. Soc.* **2000**, *20*, 1859.

[54] K.S.W. Sing, *Pure Appl. Chem.* **1982**, *54*, 2201.

[55] Gmelin, in *Gmelin Handb. Inorg. Organomet. Chem.*, Springer Verlag, Berlin **1993**, 131.

[56] OECD SIDS, *Tungsten Carbide*, **2005**.

[57] Y. Wang, C. He, A. Brouzgou, Y. Liang, R. Fu, D. Wu, P. Tsiakaras, S. Song, *J. Power Sources* **2012**, *200*, 8.

[58] Y. Wang, S. Song, P.K. Shen, C. Guo, C.M. Li, *J. Mater. Chem.* **2009**, *19*, 6149.

[59] Y. Wang, S. Song, V. Maragou, P.K. Shen, P. Tsiakaras, *Appl. Catal. B Environ.* **2009**, *89*, 223.

[60] H. Chhina, S. Campbell, O. Kesler, *J. Power Sources* **2008**, *179*, 50.

[61] Z. Wu, Y. Yang, D. Gu, Q. Li, D. Feng, Z. Chen, B. Tu, P.A. Webley, D. Zhao, *Small* **2009**, *5*, 2738.

[62] J.P. Bosco, K. Sasaki, M. Sadakane, W. Ueda, J.G. Chen, *Chem. Mater.* **2010**, *22*, 966.

[63] M. Nie, P.K. Shen, Z. Wei, Q. Li, H. Bi, C. Liang, *ECS Electrochem. Lett.* **2012**, *1*, H11.

[64] H. Ryou, J. Drazin, K. Wahl, S. Qadri, E.P. Gorzkowski, B.N. Feigelson, J.A. Wollmershauser, *ACS Nano* **2018**.

[65] B. Jiang, G.J. Weng, *Int. J. Plast.* **2004**, *20*, 2007.

[66] A.A. Onoprienko, I.B. Yanchuk, *Powder Metall. Met. Ceram.* **2006**, *45*, 190.

[67] D.A. Czaplewski, J.P. Sullivan, T.A. Friedmann, J.R. Wendt, *Appl. Phys. Lett.* **2005**, *87*, 1.

[68] R. Anton, *Carbon N. Y.* **2009**, *47*, 856.

[69] F.J. Maldonado-Hódar, C. Moreno-Castilla, J. Rivera-Utrilla, Y. Hanzawa, Y. Yamada, *Langmuir* **2000**, *16*, 4367.

[70] S.J. Sun, M.D. Zhang, *J. Mater. Sci.* **1991**, *26*, 5762.

[71] T. Tanno, A. Hasegawa, J.C. He, M. Fujiwara, M. Satou, S. Nogami, K. Abe, T. Shishido, *J. Nucl. Mater.* **2009**, *386–388*, 218.

[72] A.G. Dumanli, A.H. Windle, *J. Mater. Sci.* **2012**, *47*, 4236.

[73] D.C. Nagle, R.J. Bodnar, K.J. Livi, D. Zhang, D.H. Fairbrother, K.A. Wepasnick, Y.-R. Rhim, *Carbon N. Y.* **2009**, *48*, 1012.

[74] K. Tanaka, Y. Kamotani, Y. Yokokohji, *IEEE Int. Conf. Intell. Robot. Syst.* **2007**, 2540.

[75] A. Namiki, S. Yokosawa, *IEEE Int. Conf. Intell. Robot. Syst.* **2015**, *2015-Decem*, 5623.

[76] M. Schenk, S.D. Guest, in *Origami 5 Fifth Int. Meet. Origami Sci. Math. Educ.*, CRC Press**2011**, 291.

[77] D. Bograchev, M. Gueguen, J.C. Grandidier, S. Martemianov, *J. Power Sources* **2008**, *180*, 393.

[78] K.L. Corcoran, *CREASE AND EMBOSSING DIE*, **2005**, US 2005/0215405 A1.

[79] P.W. Jarrett, D.M. Jarrett, *ROLLERS FOR CUTTING, CREASlNG, PERFORATING OR EMBOSSING SHEET MATERIALS*, **1973**, 3,744,384.

[80] E. Cavagna, *DEVICE FOR EMBOSSING AND/OR CREASING SHEET, 0R ROLL MATERIAL*, **1987**, 4,641,575.

[81] H. Liu, J. Dai, *Rob. Auton. Syst.* **2003**, *42*, 47.

[82] C. Zhao, Q. Peng, P. Gu, *Proc. Inst. Mech. Eng. Part B J. Eng. Manuf.* **2015**, *229*, 0954405414559281.

[83] H. Celik, S. Samanli, Ö. Öney, *J. Ceram. Process. Res.* **2014**, *15*, 508.

[84] Z. Chen, M. Qin, P. Chen, B. Jia, Q. He, X. Qu, *Int. J. Hydrogen Energy* **2016**, *41*, 13005.

[85] X. Zhou, Y. Qiu, J. Yu, J. Yin, S. Gao, *Int. J. Hydrogen Energy* **2011**, *36*, 7398.

[86] Q. Cheng, Z. Song, T. Ma, B.B. Smith, R. Tang, H. Yu, H. Jiang, C.K. Chan, *Nano Lett.* **2013**, *13*, 4969.

Table of Content

Architected Tungsten Carbide (WC) electrodes were fabricated using origami and heat treatment techniques. We report the effect of different process parameters on the synthesis of WC structures from a cellulosic precursor. The WC origami structures featured low density and exhibited good mechanical strength and elastic modulus in such low density. Furthermore, these WC structures exhibited excellent electrical stability under compressive load which is highly desirable for architected electrode material.